Sascha Grusche,

"**Basic slit spectroscope reveals three-dimensional scenes through diagonal slices of hyperspectral cubes**,"

Appl. Opt. **53**, 4594-4603 (2014)

Basic slit spectroscope reveals three-dimensional scenes through diagonal slices of hyperspectral cubes

Sascha Grusche

Physikdidaktik, Fakultät 2—Pädagogische Hochschule Weingarten, University of Education, Kirchplatz 2, 88250 Weingarten, Germany (saschagrusche@gmail.com)

Received 25 March 2014; revised 29 May 2014; accepted 30 May 2014; posted 2 June 2014 (Doc. ID 208868); published 10 July 2014

A basic slit spectroscope is usually held close to the eye to produce the spectrum of a single slit view. However, a more distant viewer may have multiple slit views at once, an effect of dispersion that has been overlooked. Investigations of spectroscopic image geometry reveal that the maximum field of view equals the dispersion angle. Spectrally decoded camera-obscura projections compose three-dimensional images of a scene, emulating a Benton hologram. The images represent diagonal sections of a hyperspectral datacube. Consequently, the spectroscope can be used as an autostereoscopic display and for a fourth technique of hyperspectral data acquisition, named spatiospectral scanning.

OCIS codes: (110.0110) Imaging systems; (110.4234) Multispectral and hyperspectral imaging; (300.0300) Spectroscopy; (300.6170) Spectra; (330.0330) Vision, color, and visual optics; (330.1400) Vision - binocular and stereopsis.

http://dx.doi.org/10.1364/AO.53.004594

1. Introduction

For three centuries, slit spectroscopes have been used to disperse the image of an illuminated slit into a spectrum of colored slit images [1,2]. In the slit spectrum, each color is monochromatic, representing a specific wavelength of light [3,4]. The wavelength composition allows one to quantify color qualities [1,4], to analyze the chemical composition of substances on earth [5] and in the sky [6,7], and to infer the thermodynamics and kinematics of galaxies [8], stars [9], or even sun spots [10].

A basic slit spectroscope is a lightproof box with a slit at one end and a diffraction grating at the other [11–15]. With one's eye (or camera) close to the grating, one observes two types of virtual image. In the zeroth diffraction order, one looks straight through the slit. It reveals only a strip of the scene, which we will call a slit view. In the first diffraction order, one sees the spectrum.

The implicit notion is that this spectrum represents the slit view, split up into its monochromatic constituents, *cf.* [12]. After all, one general effect of dispersion has been persistently overlooked: Each monochromatic image in the spectrum shows a given object from a different viewpoint [16]. Consequently, a basic slit spectroscope should produce a spectral arrangement of different slit views. To test whether these slit views could compose the image of a whole scene, we explored the relationship between the geometry of the spectroscopic system and the spectroscopic image.

This paper reveals that a basic slit spectroscope is indeed capable of imaging a whole scene at once (the curious reader may peer into Section 4). A simple slit spectroscope is a three-dimensional (3D) imaging device in disguise, with potential applications in autostereoscopic 3D display and 3D spectroscopy.

In Section 2, I analyze the imaging process to predict the geometric features of spectroscopic images. In Section 3, horizontal and vertical setups are

1559-128X/14/204594-10$15.00/0

presented. In Section 4, the spectroscopic images are described. In Section 5, I discuss the implications, limitations, and applications of the study. In Section 6, the main ideas and findings are summarized.

2. Spectroscopic Image Geometry

A. Camera Obscura and Slit View Combined

As in a basic spectroscope [11–15], the setup comprises a slit aperture A (with slit width w) and a grating G (with grating period g) with lines parallel to the slit. To understand the spectroscopic image in the first diffraction order, let us analyze the imaging process in two orthogonal planes; see Fig. 1.

In a plane perpendicular to the slit aperture A, all rays pass a pinhole, yielding a camera-obscura projection on the grating [14]. We will call this plane the camera-obscura plane, see Fig. 1(a).

In this camera-obscura plane, differently colored rays connect different object points with the viewer's eye. Correspondingly, each object point is seen from the direction of a wavelength-specific virtual viewer. For an actual viewer at a viewing distance d_I from the grating, we find the position of each virtual viewer by following the incident ray from each object point and retracing it a distance d_I beyond the grating, *cf.* [17]. With the specific geometry of Fig. 1, the actual viewer sees an extended scene from the same direction as the virtual viewer of the blue ray, *cf.* Section 5.C. The image is a spectrally decoded camera-obscura projection.

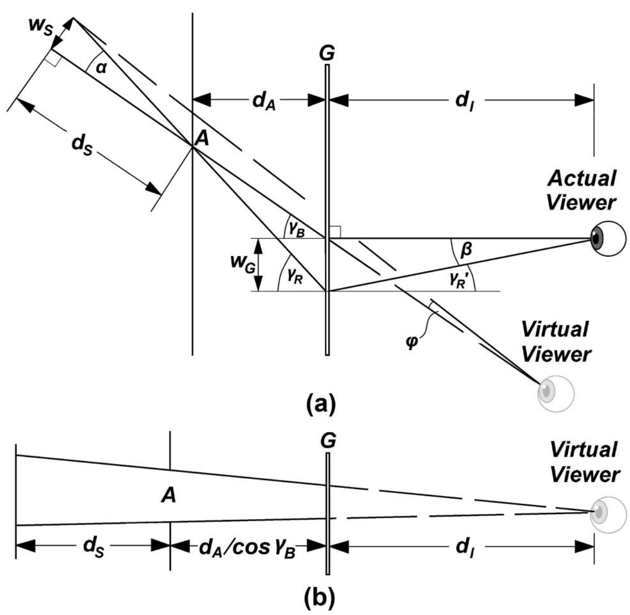

Fig. 1. Ray geometry for the spectroscopic system with slit aperture A, grating G, and a viewer looking at an object at a distance d_S. (a) Camera-obscura plane. With the grating, the viewer spectrally decodes a camera-obscura projection. For clarity, only the outermost rays to the viewer are shown. α: field of view; β: actual visual angle; φ: virtual visual angle; γ_B: incident angle of blue ray; γ_R: incident angle of red ray; γ_R': diffraction angle of red ray. (b) Slit-view plane for the blue rays. The rays are undeflected because the grating lines lie parallel to the slit-view plane.

In a plane parallel to the slit aperture A, rays connect object points and the virtual viewer's eye directly, yielding a single slit view. We will call this plane the slit-view plane; see Fig. 1(b).

Let us now synthesize the imaging processes from the camera-obscura plane and the slit-view plane. Dispersion at the grating allows the viewer to look through the slit in multiple directions at once. The resulting spectrum is an arrangement of different slit views. Under broadband illumination, a potentially continuous image of a scene is formed by the differently colored rays.

B. Field of View and Visual Angles

With our ray geometry from Fig. 1(a), we may predict the field of view α, the actual visual angle β, and the virtual visual angle φ. Here, α determines how much of a scene is visible at once; β determines the apparent size of the scene, and φ is the angle under which the virtual viewer would see that scene in direct view. For simplicity, we assume that the outermost blue ray (at wavelength λ_B) to the viewer's eye has a diffraction angle $\gamma_B' = 0$ at the grating. The well-known grating formula requires this blue ray to be incident on the grating at an angle

$$\gamma_B = \arcsin\left(\frac{\lambda_B}{g}\right). \tag{1}$$

For a field of view α, the outermost red ray (at wavelength λ_R) must be incident on the grating at an angle

$$\gamma_R = \gamma_B + \alpha. \tag{2}$$

The angle of the observed red ray equals the actual visual angle

$$\beta = \gamma_R' = \arcsin\left(\frac{\lambda_R}{g} - \sin\gamma_R\right) \geq 0. \tag{3}$$

With the grating at a distance d_A from the aperture, the outermost rays form two triangles. Their common base has width

$$w_G = (\tan\gamma_R - \tan\gamma_B)d_A = d_I \tan\beta. \tag{4}$$

Thus, the viewing distance d_I affects the actual visual angle

$$\beta = \arctan\left(d_A \frac{\tan\gamma_R - \tan\gamma_B}{d_I}\right). \tag{5}$$

As the viewer recedes along the blue ray, the red ray becomes almost parallel to it. The field of view approaches a maximum:

$$\lim_{d_I \to \infty} \alpha = \alpha_{\max} = \arcsin\left(\frac{\lambda_R}{g}\right) - \arcsin\left(\frac{\lambda_B}{g}\right). \quad (6)$$

Reinterpreting Eq. (6) as the angle between diffracted red and blue rays with normal incidence, we define the dispersion angle:

$$\delta := \gamma'_R(\gamma_R = 0) - \gamma'_B(\gamma_B = 0). \quad (7)$$

Then, the maximum field of view equals the dispersion angle

$$\alpha_{\max} = \delta. \quad (8)$$

This angle solely depends on the grating period g and the spectral range $S = [\lambda_B; \lambda_R]$ of the incident light. A grating with $1/g = 1000$ lines/mm yields $\alpha_{\max} \approx 0.36\ \text{rad} \mathrel{\hat{=}} 20.8°$ for $S = [400\ \text{nm}; 700\ \text{nm}]$, and $\alpha_{\max} \approx 0.30$ rad for $S = [420\ \text{nm}; 670\ \text{nm}]$.

The scene appears to the actual viewer under a visual angle β that usually differs from the virtual viewer's φ. For a scene of width $w_S = \tan \alpha d_S$, the virtual visual angle is

$$\varphi = \arctan\left(\frac{w_S}{d_S + d_A / \cos \gamma_B + d_I}\right). \quad (9)$$

For a first overview, let us plot the visual angles and field of view against viewing distance. With no straightforward way to calculate $\alpha = \alpha(d_I)$, we work backwards: First, for a set $\{\alpha_n\}$ of given values of α (where $0 \le \alpha_n \le \alpha_{\max}$), we compute the values $\beta_n = \beta(\alpha_n)$ via Eqs. (2) and (3). Second, with Eq. (4), we obtain the corresponding values of $d_{I,n} = d_I(\beta_n)$ and, together with Eq. (2), values of $d_{I,n} = d_I(\alpha_n)$. Third, with Eq. (9), we find values of $\varphi_n = \varphi(d_{I,n})$. Finally, we plot the values of α_n, β_n, and φ_n versus the values of $d_{I,n}$, and interpolate, as in Fig. 2. With such a graph, we can systematically predict how much of a scene is visible and how the image is proportioned.

C. Image Proportions, Magnification, and Perspective

Image size is determined by visual angle. In the slit-view plane, image size is normal because the virtual viewer's visual angle always matches the actual viewer's. In the camera-obscura plane, however, image size is normal only if $\varphi = \beta$, *cf.* Figs. 1(a) and 2.

Based on Eqs. (5) and (9), we can satisfy the condition $\beta = \varphi$ for only one set of distances (d_S, d_A, d_I) at a time. If these distances are not mutually adjusted, the actual visual angle β will differ from the virtual visual angle φ, causing angular magnification along the spectrum:

$$M_S = -\frac{\tan \beta}{\tan \varphi}. \quad (10)$$

(Conventionally, the minus sign indicates that, in the camera-obscura plane, the image is inverted. This inversion can be reversed via reflection, *cf.* Section 3.A.)

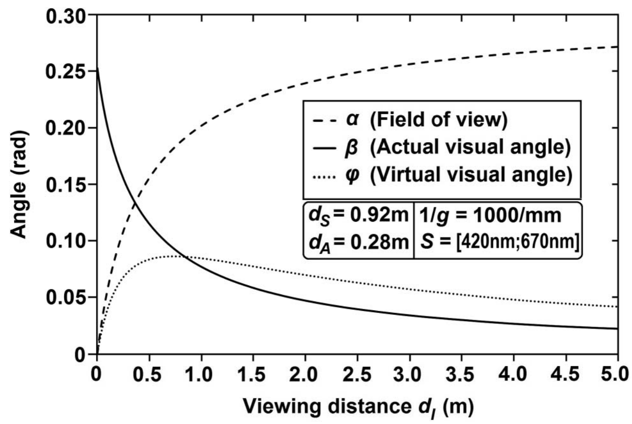

Fig. 2. Angles predicted for still-life situation. Parameters are the length of the spectroscope d_A, its distance d_S from the scene, its grating period g, and the spectral range S. A viewer directly at the spectroscopic grating G ($d_I \approx 0$ m) sees a wide spectrum ($\beta \approx 0.25$ rad) of a single slit view ($\alpha \approx 0$ rad). With increased viewing distance, the spectrum should become narrower while representing a wider field of view. At a distance $d_I \approx 0.8$ m from the grating G, where $\beta = \varphi$, the image should have correct proportions.

The magnification along the spectrum stems from a hybrid of two perspectives: In the slit-view plane, the perspective has its center of projection at the virtual viewer's position; see Fig. 1(b). In the camera-obscura plane, however, the center of projection is the aperture A; see Fig. 1(a). The two perspectives become similar as the centers of projection approach each other. In other words, if objects at a distance d_S undergo a given magnification, more distant objects will undergo a similar magnification, provided that $(d_A + d_I)/d_S \to 0$. This is the case for distant scenes with small parallax, such as a landscape.

3. Setup Realizations and Observation Methods

A. Horizontal-Slit Spectroscope

To test our quantitative predictions, a horizontal-slit spectroscope—see Fig. 3(a)—was built from two large metal plates as a slit aperture (thickness: 1 mm, slit width $w = 1$ mm), and a grating ($d_A = 28 \pm 0.2$ cm; $1/g = 1000$ lines/mm, available at AstroMedia Germany, size ca. 14 cm × 15 cm, worth 7€≙$10, held between two glass plates, each 1.5 mm thin). In front of it, a still life was set up. It was composed of a white paper strip with black, 2.0 ± 0.5 mm thick centimeter-scale marks, placed vertically at $d_S = 92 \pm 2$ cm for calculating the visual angle; a white modeling clay figure and a tilted, beige cup with blue ornaments for evaluating the three-dimensional effect; a Styrofoam ball for quantifying magnification along the spectrum; a toy police car for investigating parallax; and a black background for contrast. The still life was illuminated sideways with broadband white light from a nearby video projector (*acer* P7215; $S = [420 \pm 10\ \text{nm}; 670 \pm 10\ \text{nm}]$; luminous flux: 6000 lumens—caution: nearby objects may heat

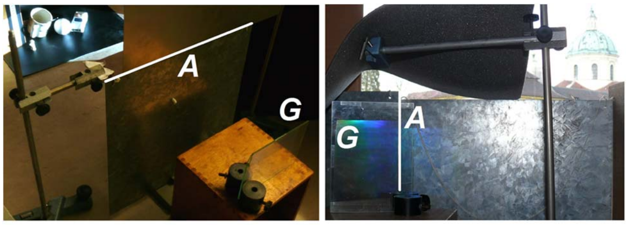

Fig. 3. Basic spectroscopes. A: slit aperture (emphasized by a white line); G: grating. (a) Horizontal-slit spectroscope (with mirror just above A) for still life at top left. (b) Vertical-slit spectroscope for basilica at top right.

up and melt or smolder). A narrow mirror was horizontally attached outside the spectroscope, just above the slit, to obtain an upright image; see Fig. 3(a).

To document how both the field of view and angular magnification vary with viewing distance, a Sony Ericsson phone camera MT15i was used (relative aperture: $f/2.4$; exposure time: 1/16 s). Unlike a camera with a larger objective, the cell phone camera faithfully records the viewer's perspective. Experimental values for angular magnification M_S were calculated via the height-to-width ratio of the images of the Styrofoam sphere. The relative heights and widths were obtained in Microsoft Paint by fitting an ellipse onto each image and reading off the pixel numbers.

To investigate how the spectroscopic image changes when moving transverse to the slit, a Panasonic camera DMC-FZ50 (63 ± 1 cm behind the grating; relative aperture: $f/11$; exposure time: 6 s) was raised or lowered with wooden plates underneath it (each 22 ± 1 mm thick). The camera height h was defined to be zero where the complete still life was visible (up being positive).

To demonstrate the horizontal parallax of the spectroscopic image, it was photographed with the Panasonic camera (63 ± 1 cm behind the grating) from two positions 23 cm horizontally apart.

B. Vertical-Slit Spectroscope

To try the spectroscope with daylight, two metal plates were placed at the author's office window to form a vertical slit (width $w = 1$ mm, length $l = 46$ cm) before the grating ($1/g = 1000$ lines/mm; $d_A \approx 20$ cm). The setup was shielded against stray light; see Fig. 3(b). With a Panasonic DMC-FZ50 about 40 cm behind the grating (relative aperture: $f/11$; exposure time: 1 s), photos were taken through the spectroscope toward the basilica of Weingarten (its tower being 20 ± 2 m wide, centered at $d_S = 170 \pm 5$ m, as measured in Google Maps). Unlike in Section 3.A, no mirror was built into the spectroscopic system.

To test angular magnification at different object distances, a similar spectroscope was used ($d_A = 14 \pm 0.2$ cm, $1/g = 1000$ lines/mm, $w = 1$ mm) for convenient measurement of precise angles and distances on a table. (Again, no mirror was installed.) A wooden sphere (45 ± 1 mm in diameter) was backlit by the video projector via a translucent screen. The distance from the sphere's center to the slit was decreased from $d_S = 100 \pm 0.5$ cm to $d_S = 12.5 \pm 0.5$ cm. Photos were taken with a Sony Ericsson phone camera MT15i at $d_I = 50 \pm 0.5$ cm (relative aperture: $f/2.4$; exposure time: 1/16 s). To avoid overexposure, the video projector was dimmed by projecting gray with red, green, and blue components (R|G|B) = (127|127|127) instead of white (R|G|B) = (255|255|255). Experimental values for angular magnification M_S were calculated via the width-to-height ratio of the sphere's images.

4. Spectroscopic Image Results

A. Horizontal-Slit Spectra

As the viewing distance to the grating was increased, the abstract spectrum of a single slit view was transformed into a concrete image of the entire scene; see Fig. 4. The still life appeared correctly proportioned at a viewing distance $d_I = 85 \pm 5$ cm. Before that, it appeared vertically stretched ($|M_S| > 1$); see Figs. 4(a)–4(e). Beyond that, it appeared vertically squashed ($0 < |M_S| < 1$); see Fig. 4(f). At 2 m, the field of view was $\alpha = 220 \pm 20$ mrad, but the still life appeared contracted by one third ($|M_S| \approx 2/3$). The centimeter-scale marks always appeared evenly spaced.

Changing the viewing height revealed different spatial and spectral parts of the scene. Meanwhile, the perspective appeared fixed; see Fig. 5. Accordingly, no vertical parallax was observed.

Binocular vision through the horizontal-slit spectroscope felt natural and easy, producing sharp, 3D images. While the 2 mm thick scale marks were clearly visible, horizontal lines 1 mm thin were invisible. In the monochromatic direction, image sharpness was normal. The spectroscopic image had continuous horizontal parallax; see Fig. 6.

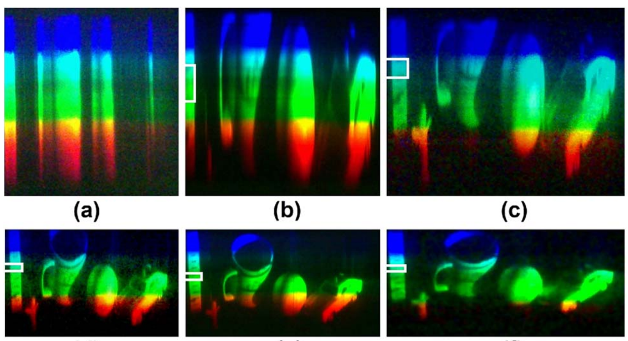

Fig. 4. Increasing the viewing distance d_I increases the field of view α, while decreasing the absolute value of angular magnification $|M_s|$ (in the vertical direction). The scale (left) indicates α (1 unit = 1 cm$\hat{=}$10 mrad, emphasized by a white frame). (a) $d_I = 0$ m; $\alpha \approx 0$. (b) $d_I = 10 \pm 0.5$ cm, $\alpha = 55 \pm 5$ mrad; $|M_S| = 4.75 \pm 0.1$ (c) $d_I = 20 \pm 0.5$ cm, $\alpha = 105 \pm 8$ mrad; $|M_S| = 2.9 \pm 0.1$. (d) $d_I = 50 \pm 1$ cm, $\alpha = 145 \pm 10$ mrad; $|M_S| = 1.72 \pm 0.05$. (e) $d_I = 75 \pm 1$ cm, $\alpha = 172 \pm 10$ mrad; $|M_S| = 1.27 \pm 0.05$. (f) $d_I = 100 \pm 1$ cm, $\alpha = 190 \pm 10$ mrad; $|M_S| = 0.93 \pm 0.03$.

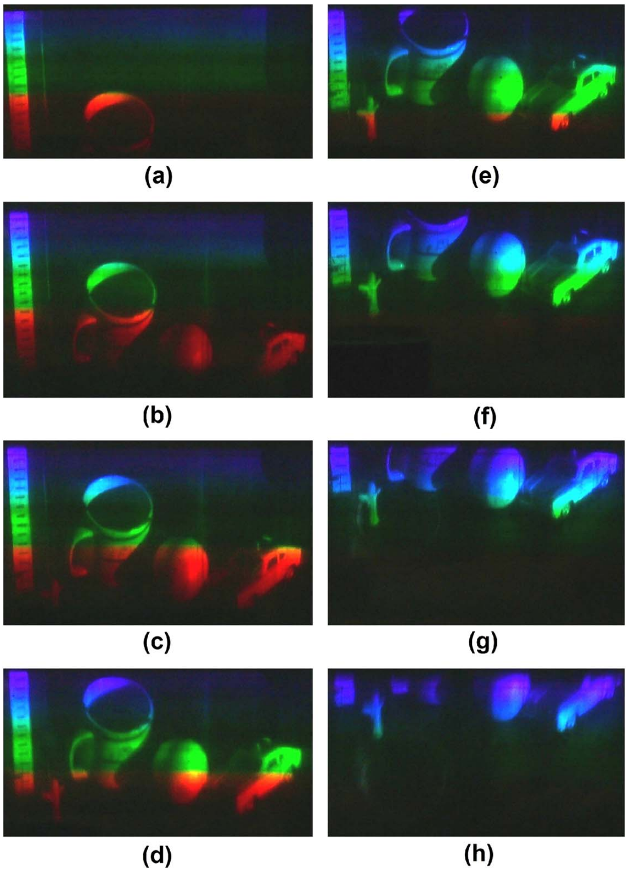

Fig. 5. Changing the viewing height h reveals different parts of the scene but from the same perspective. (a) $h = +8.8$ cm. (b) $h = +4.4$ cm. (c) $h = +2.2$ cm. (d) h:=0 (e) $h = -2.2$ cm. (f) $h = -4.4$ cm. (g) $h = -6.6$ cm (h) $h = -8.8$ cm.

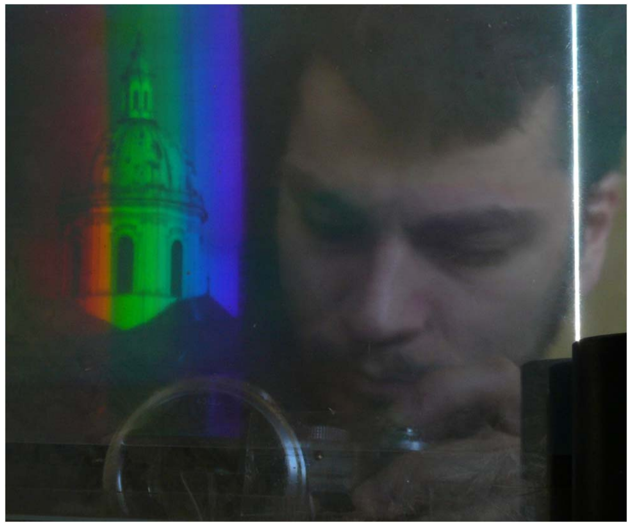

Fig. 7. High-resolution spectroscopic image of the basilica before the author's office window. The camera and photographer are reflected in the glass that holds the grating. The slit appears as a bright line on the right.

B. Vertical-Slit Spectra

The basilica was clearly visible both under direct and diffuse sunlight. Even details—decorative molding on the tower, nearby scaffold bars—were resolved along both image axes, *cf.* Fig. 7. In the photographed spectroscopic image, the field of view was $\alpha = 10 \pm 1°$ (based on the width and distance of the basilica tower).

Along the horizontal direction, each image spot had a fixed position on the grating, independent of the position of the viewer or the spectrum. Although the spectral color bands were slightly bent, *cf.* Figs. 7 and 8, the image had no spatial distortions.

With no mirror at the slit, left and right were reversed. Moving the head rightward moved the spectrum rightward, thereby shifting the view toward the left part of the scene, and vice versa. Unlike monocular vision, binocular vision tended to produce double images and visual fatigue with the vertical-slit setup.

The absolute value of angular magnification $|M_S|$ increased with decreasing object distance. For a given viewing distance, correct proportions arose only at a specific object distance. A more distant object appeared horizontally squashed ($0 < |M_S| < 1$); see Figs. 8(a)–8(c). A closer object appeared horizontally stretched ($|M_S| > 1$); see Figs. 8(d) and 8(e); *cf*. Fig. 9. With no mirror in the spectroscopic system, left and right were reversed: When the object was moved to one side, its image moved to the other.

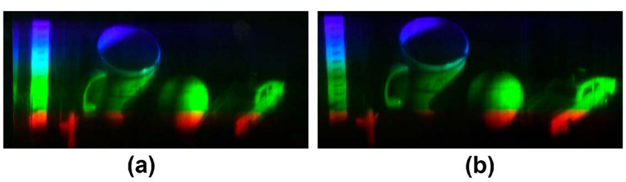

Fig. 6. Parallax parallel to the slit. (a) Left-eye view. (b) Right-eye view.

5. Discussion

A. Relation to Similar Imaging Systems

As predicted, a basic slit spectroscope displays a whole scene at once, if the viewer is not too close to the grating. Figuratively speaking, an image of the scene is carved from the spectrum of the light source. (Technically speaking, the spectrum of the light source is locally darkened according to the light absorption and shadow distribution in the observed scene.) We can understand this by relating the spectroscope to similar imaging systems.

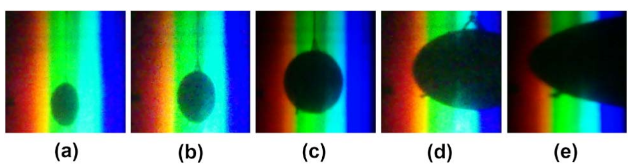

Fig. 8. The absolute value of angular magnification $|M_s|$ (along the horizontal direction) increases as the sphere's distance d_s to the slit is reduced, *cf.* Fig. 9. (a) $d_S = 100 \pm 0.5$ cm, (b) $d_S = 75 \pm 0.5$ cm, (c) $d_S = 50 \pm 0.5$ cm, (d) $d_S = 25 \pm 0.5$ cm, (e) $d_S = 12.5 \pm 0.5$ cm.

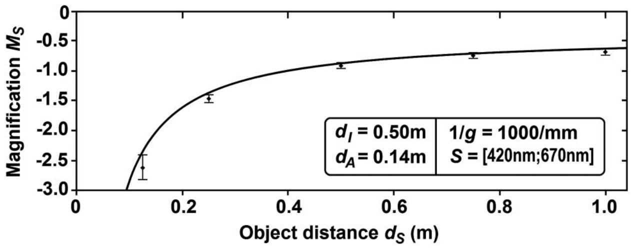

Fig. 9. Experimental values for angular magnification from Fig. 8 (data points with error bars for measurement uncertainties) confirm the theoretical values from Eq. (10) (solid line).

Without the slit, the scene behind the grating appears blurry in the first diffraction order [16,17]. Here, one sees a composite of mutually displaced, monochromatic images [3,18]. Each represents the complete scene from a different perspective [16]. Likewise, a slit between the scene and the grating is imaged at different positions, appearing blurry. Paradoxically, a sharp image of the scene emerges. Here, one sees a composite of mutually displaced, monochromatic slit images, *cf.* [19]. Each represents a different view through the slit.

We may reinterpret this setup as a modified camera obscura, *cf.* [14]. The slit acts as a series of pinholes, whereas the grating acts as a screen for a series of projections. However, the grating diffracts the rays only into wavelength-specific directions. Hence, each projection contributes only a linear, rainbow-colored segment to the spectroscopic image, as implied by Fig. 1(b).

Adding a grating in front of the spectroscope leads to a double-diffraction setup with a slit in between [20,21]. Whereas the front grating spectrally encodes different views of an object, the back grating spectrally decodes these as a depth-inverted image. A normal-depth image has previously been obtained by viewing the opposite diffraction order [22]. Now, we have produced normal-depth images by removing the front grating. This grating is neither essential for imaging nor necessary for magnifying an object along the spectrum. Both effects are achieved by the camera-obscura process at the slit. Conversely, parallax is reduced to the direction parallel to the slit because a camera-obscura projection has a fixed perspective.

Replacing the slit aperture with a linear light source behind the object leads to a 3D shadow display [23]. However, the spectroscope has three advantages: First, it is not limited to producing silhouettes. Second, it does not invert the object proportions from front to back, because it features camera-obscura projections instead of rear-projections. Third, the slit width can be adjusted for image sharpness.

Exchanging the slit with a linear Projected-Image Circumlineascopy (PICS) screen [19] leads to striking image similarities. First, moving transverse to the slit is analogous to moving the PICS screen transverse to the projection beam. Second, the width w_A of a spectrally decoded PICS image is proportional to the distance d_A from the linear screen to the dispersive element. Similarly, on the spectroscopic grating, the width w_G of the spectrally decoded camera-obscura projection is proportional to the distance d_A from the slit to the grating.

Contrary to PICS [19], spectroscopic image proportions also depend on the viewing distance d_I, because the spectroscopic image is composed of viewpoint-specific slit views. For the same reason, the light from the slit lacks the mirror-immunity that is unique to PICS. This allowed us to reverse the image inversion along the spectrum; see Section 3.A.

B. Image Position, Accommodation, and Astigmatism

In the slit-view plane, the virtual image hovers at the same distance as the scene (based on accommodation, perspective, and parallax), *cf.* [17]. In the camera-obscura plane, however, a real projection lies on the grating. With a vertical-slit setup, the eyes must converge on the grating while accommodating beyond it. Double images and visual fatigue ensue. This cannot occur with a horizontal-slit setup, where the lines of sight converge at the distance of the scene.

Accidentally, the viewer may accommodate on the slit instead of the scene, as is intentionally done in a basic spectroscope when reading the wavelength scale against the spectrum [12]. Accommodating on the scene is easier in a horizontal-slit spectroscope. Here, horizontal parallax might give a focusing cue that is missing in a vertical-slit setup.

Astigmatism arises because light is diffracted only in the camera-obscura plane, *cf.* [21]. After diffraction, rays diverge at a different angle than before. Hence, the light bundle to the eye pupil has a different divergence angle in the camera-obscura plane than in the slit-view plane. A normal eye lens cannot bring such a bundle to a single focus. The astigmatism was inconspicuous because the divergence angle varies only slightly.

C. Limitations

To simplify the discussion of image geometry, we have assumed that the observed blue ray is orthogonal to the grating. Other viewing directions cause quantitative discrepancies. The experimental values are congruent with the theoretical values only because we tried to make our setups congruent with Fig. 1. We only treated setups where the grating is neither rotated nor tilted relative to the slit aperture.

Achieving the maximum field of view requires an infinite viewing distance, which cannot be achieved except with a lens system; see Section 5.D. At least, the correctly proportioned still-life image already represented 65% of the maximum field of view. Moreover, one can increase the effective field of view manifold by moving transverse to the slit, as Fig. 5 shows.

D. Suggested Applications

1. *Emulation of Rainbow Holograms*

The spectroscopic images have three things in common with (Benton) rainbow holograms [24].

First, they appear 3D. Second, they represent only one slit view if viewed with monochromatic light, yet a whole scene if viewed with broadband light. Third, they have motion parallax along the monochromatic direction.

Stereoscopic images emerge only with a horizontal-slit setup, where each eye sees the scene from a different angle. With a vertical-slit setup, the image is nonstereoscopic because it lacks horizontal parallax. Still, it looks 3D thanks to vertical motion parallax and variable accommodation.

Although basic spectroscopy is simpler than rainbow holography, even the setup geometry is similar. To emulate a 360° rainbow hologram [25–27], simply illuminate an object with a broadband light source and surround both with a cylindrical, horizontal-slit spectroscope. With 3D printing on the rise, this basic spectroscopy offers a cheap alternative to rainbow holography, especially for moving images. Even a 2D anaglyph image, through a vertical-slit spectroscope, appears as an autostereoscopic image (due to spectral decoding), as we will show elsewhere. Hologram emulations are applicable in entertainment, education, art, and advertisement.

2. A Fourth Technique of Hyperspectral Imaging

Each spectroscopic image represents a thin diagonal slice of a hyperspectral datacube, *cf.* Figs. 5 and 10. In the existing hyperspectral imaging techniques—nonscanning, spectral scanning, and spatial scanning—"the datacube is sliced along orthogonal dimensions" [28], see Figs. 10(a)–10(c). There has been no technique for diagonal slicing, "since it is not easy to rotate a slice within the cube" [28]. This gap was pointed out only a few years ago [28]. Since then, interference filters have been used to chop the cube into slanted slabs, but these slabs are undesirably short, thick, and uneven (with small spectral range and low spectral resolution) [29–31]. Closest to diagonal slicing is spectrally encoded endoscopy, but it yields only lines instead of planes [32]. Thus, the gap has remained [33], *cf.* [34–37]. To fill this gap, we introduce a fourth basic technique of hyperspectral imaging; see Fig. 10(d). For the proposed spatiospectral scanning, we simply move a camera transverse to the slit of a basic spectroscope; see Fig. 11.

The proposed spatiospectral scanning unites the complementary properties of spatial and spectral scanning. Whereas spectral scanning makes it easy to map the spectral data onto the spatial (x, y) coordinates, it requires a platform that does not move relative to the scene. Conversely, spatial scanning allows for a mobile platform, but the question is how to construct (from the slit spectra) a spatial (x, y) map of the scene, especially if the relative velocity of the platform varies over time.

Combining the individual strengths of spectral and spatial scanning, spatiospectral scanning compensates the corresponding weaknesses. Both static and mobile platforms are possible: Either the camera

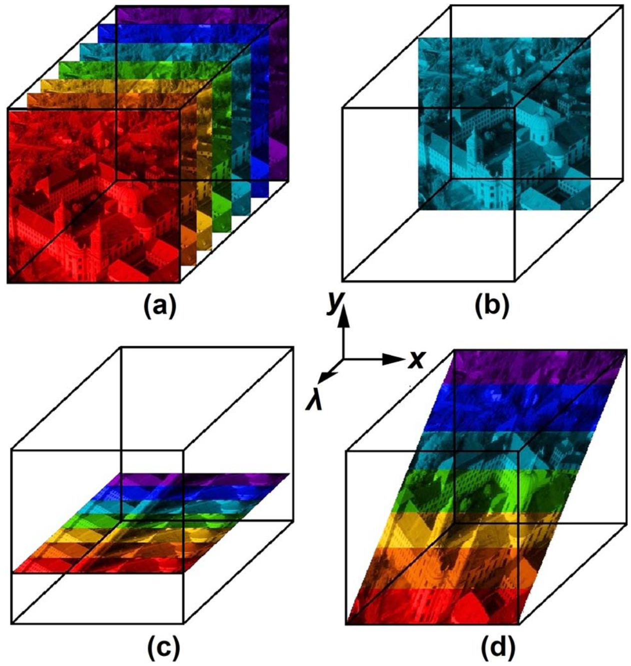

Fig. 10. Introducing a fourth hyperspectral imaging technique. The datacube represents two spatial dimensions (x, y) and one spectral dimension (λ) of a scene. (a) Nonscanning techniques produce a chromatically dispersed snapshot of the scene. (b) Spectral scanning techniques produce a temporal sequence of monochromatic images of the scene. (c) Spatial scanning techniques produce a temporal sequence of ordinary slit spectra for strips of the scene. (d) The proposed spatiospectral scanning technique produces a temporal sequence of spectrally coded images of the scene. Note: As the slit is widened, (d) becomes (a). As the viewing distance d_I approaches zero, (d) becomes (c), *cf.* Fig. 4.

alone or the entire system is moved transverse to the slit. Moreover, each image represents the scene in its two spatial dimensions, one of which is spectrally

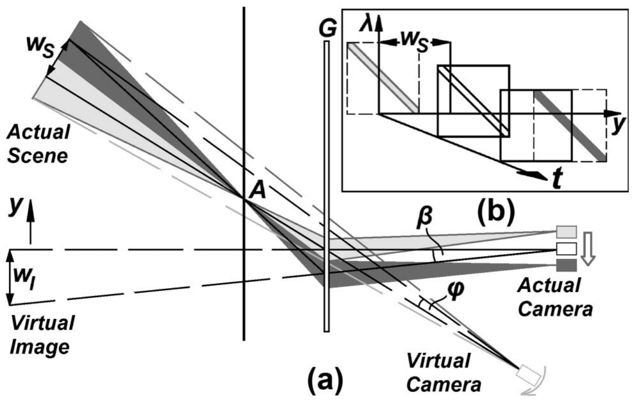

Fig. 11. Spatiospectral scanning, shown in the camera-obscura plane. (a) While the actual camera is moved transverse to the slit A, the recorded virtual images represent the actual scene as if photographed from the direction of a virtual camera that is tilted. If $\beta = \varphi$, the virtual image has the same width $w_I = w_S$ as the actual scene. (b) Shifting the camera produces a sequence (in time t) of diagonal slices of the hyperspectral datacube, as in Fig. 10(d), *cf.* Fig. 5; x-dimension not shown. Each symbolic shade of gray relates each image to the corresponding camera position and spectrally diverse light bundle in (a).

coded as $y = y(\lambda)$; see Fig. 10(d). Hence, the spectral data are easily mapped onto the objects in the scene, even if the scanning path is irregular or irretrievable. Tying spatial and spectral scanning together, spatiospectral scanning is more flexible and reliable in application than either of the two alone.

Let us now discuss spatial and spectral resolution along the direction $y = y(\lambda)$ of the spectrum, based on Fig. 12. For practical purposes, we assume that the camera is at a distance d_I where the spectroscopic image is correctly proportioned ($\beta = \varphi$). For maximum spectral resolution, the camera needs to have a point-like entrance pupil [14,15], so we model it as a pinhole camera (neglecting diffraction).

The finite width w of the spectroscopic slit A causes an object point to be projected onto the grating G as an image spot of finite width Δw_G; see Fig. 12. According to the intercept theorem, the width of each image spot is

$$\Delta w_G = \left(1 + \frac{d_A}{d_S \cos \gamma_B}\right) w. \quad (11)$$

The width Δw_G of each image spot causes a visual widening of each object point, which we will denote Δy. This visual widening Δy relates to the total width w_S of the scene (approximately) as the width Δw_G of an image spot relates to the total width w_G of the spectrally decoded projection on the grating (*cf.* Fig. 1):

$$\frac{\Delta y}{w_S} \simeq \frac{\Delta w_G}{w_G}. \quad (12)$$

The ratios from Eq. (12) become equal as the projection angle $\Delta\alpha$ in Fig. 12 approaches zero.

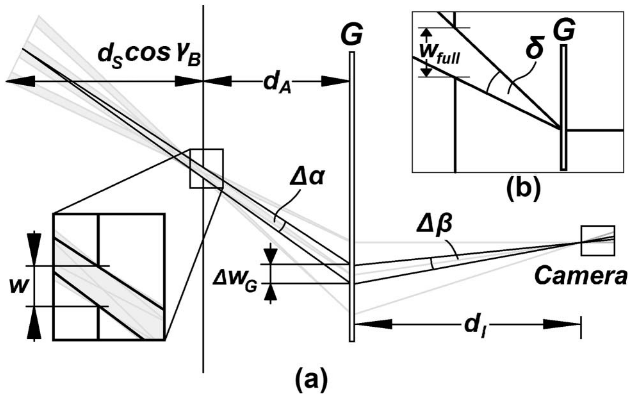

Fig. 12. Ray diagram for spatiospectral resolution, *cf.* Fig. 1. (a) Rays from a single object point diverge (black) toward the grating, forming an image spot with an apparent size $\Delta\beta$ that determines spatial resolution. Simultaneously, rays from various object points converge (gray) toward a single point on the grating, thus determining spectral resolution. (b) Each ray that exits the grating has a spectral width that is proportional to the slit width w. If $w = w_{\text{full}}$, a single ray may comprise the full spectrum.

Combining Eqs. (11) and (12), we obtain the visual widening

$$\Delta y(\beta = \varphi) = \frac{d_S \tan \alpha}{d_I \tan \beta}\left(1 + \frac{d_A}{d_S \cos \gamma_B}\right) w. \quad (13)$$

By definition, two adjacent object points are resolved if their image spots overlap halfway. Accordingly, the smallest resolvable spatial feature has width

$$w_{\text{res}}(\beta = \varphi) := \frac{\Delta y}{2}. \quad (14)$$

Furthermore, the finite width w of the spectroscopic slit causes multiple rays to exit the grating as a single ray. Comprising multiple wavelengths, that single ray has a spectral width $\Delta\lambda$. Such a ray may be composed of the full spectrum $S = [\lambda_B; \lambda_R]$ if the relevant rays from the slit converge at about the dispersion angle δ; see Fig. 12(b), *cf.* Eq. (7). This may happen if the slit has the full width

$$w_{\text{full}} \simeq \left[\tan\left(\arcsin \frac{\lambda_R}{g}\right) - \tan\left(\arcsin \frac{\lambda_B}{g}\right)\right] d_A. \quad (15)$$

Equation (15) becomes an equality for a ray that exits along the grating normal, based on Eq. (7). Narrowing the slit reduces the number of rays that may converge into a single ray. As Newton already argued in Proposition IV, Problem I of his *Opticks* [1], the spectral width relates to the full spectrum as the slit width relates to the full slit width:

$$\frac{\Delta\lambda}{\lambda_R - \lambda_B} = \frac{w}{w_{\text{full}}}. \quad (16)$$

The spectral width $\Delta\lambda$ is roughly the same for all rays that exit the grating because dispersion is roughly linear, *cf.* Figs. 4, 7, and 8; *cf.* [12]. From Eqs. (15) and (16), we obtain the spectral width

$$\Delta\lambda(\beta = \varphi) := \frac{\lambda_R - \lambda_B}{\left[\tan\left(\arcsin \frac{\lambda_R}{g}\right) - \tan\left(\arcsin \frac{\lambda_B}{g}\right)\right] d_A} w. \quad (17)$$

Based on Eqs. (14) and (17), spectral resolution is directly proportional to spatial resolution. High spatiospectral resolution is achieved with a narrow slit. In our still-life situation ($w = 1$ mm), the smallest resolvable spatial feature has width $w_{\text{res}} \approx 5$ mm, based on Eq. (14). (For obliquely incident light, the aperture's finite thickness makes the slit width effectively smaller than w. In our case, w_{res} is reduced to about 3 mm.) This explains why horizontal lines narrower than the scale marks were invisible. In this example, the spectral width is $\Delta\lambda \approx 2$ nm, based on Eq. (17). Remember that Eqs. (14) and (17) are only valid for a camera with a point-like entrance pupil, such as a phone camera [14], a webcam [15], or a miniature surveillance camera. The formulas are still approximately correct for the human eye and for a camera with comparably small aperture. As with any hyperspectral imager, spatial and spectral resolutions vary with the width of the camera's entrance pupil, and the pixel resolution of the sensor.

If the camera alone is moved, all images have the same hybrid perspective (*cf.* Section 2.C), as in Fig. 5. After all, the virtual camera is merely tilted in the camera-obscura plane; see Fig. 11(a). The hybrid character is not noticeable if the scene has little parallax or if its depth is limited (compared to the average object distance d_S). Then—for all objects at once—the distance parameters d_A and d_I can be adjusted toward $|M_S| = 1$, using Eqs. (1)–(5), (9), and (10), as in Figs. 5 and 6. Such a stationary platform with a movable camera may be applicable in all areas of hyperspectral imaging, from biomedical imaging [14] to remote sensing, *cf.* [31].

If the spectroscope is moved together with the camera, the images will differ along the y-axis. After all, the slit is shifted transverse to the scene, creating different projections in the camera-obscura plane. The difference is not noticeable if the scene has little motion parallax. Hence, the mobile imaging platform is especially suitable for remote sensing.

The basic slit spectroscope may serve as a prototype for advanced imaging platforms. For example, collecting lenses and a direct-vision prism could be added, as in Fig. 13. Thanks to the lens system, the images would have normal (instead of hybrid) perspective, and the field of view would be equal to the dispersion angle of the prism, analogous to Eq. (7). Increased light throughput would minimize exposure time, thus maximizing the speed of data acquisition. By removing the prism, one could switch from spatiospectral scanning to spatial scanning. In both scanning modes, the same amount of light would hit the sensor (only from different parts of the scene). These potential advancements highlight the simplicity, flexibility, and efficiency of spatiospectral scanning.

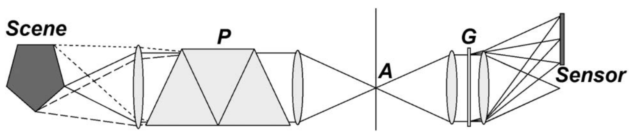

Fig. 13. Lens-based hyperspectral imager, modeled on the pinhole-based slit spectroscope. Without prism P, a single strip of the scene (solid rays) is imaged, being dispersed by grating G into a slit spectrum on the sensor, as in [38]; *cf.* Fig. 10(c). With prism P, multiple strips of the scene (dashed rays) are spectrally encoded at aperture A, being decoded by grating G as a spatiospectral image on the sensor, *cf.* Fig. 10(d).

6. Conclusion

Only now—three centuries after Newton's invention—have we discovered that a basic spectroscope can display a whole scene at once. For this insight, we literally had to take a step back.

As we recede from the spectroscopic grating, the field of view increases toward the dispersion angle. Dispersion at the grating allows a viewer to peer through the slit in multiple directions at once. In other words, spectrally decoded camera-obscura projections compose a viewpoint-specific image. The rainbow-colored image has continuous parallax parallel to the slit, emulating a Benton hologram.

Moving transverse to the slit yields thin diagonal slices of a hyperspectral datacube. Therefore, we propose a spatiospectral scanning technique for hyperspectral data acquisition. Both static and mobile platforms are applicable, and a spatial map of the scene is embedded in each spectrum. The narrower the spectroscopic slit, the higher the spatiospectral resolution. Using a basic spectroscope as a prototype, advanced setups can be designed for the proposed spatiospectral scanning technique.

Yielding a datacube, hyperspectral imaging is also called 3D spectroscopy. In hindsight, we may take this abstract term literally: Spectroscopy can produce concrete images with three spatial dimensions.

I am grateful to Prof. Dr. Florian Theilmann for inviting me in 2010 to explore spectra with him, for taking the photos for Figs. 4 and 8, and for commenting on the manuscript. I also thank Sebastian Hofmann and Marc Moosmann, who assisted me during some experiments. Moreover, I appreciate the reviewers' encouraging and constructive feedback. Finally, I thank Prof. Matthew Bershady for sharing his overview on 3D spectroscopy.

References

1. I. Newton, *Opticks: Or, a Treatise of the Reflexions, Refractions, Inflexions and Colours of Light*, 4th ed. (Dover, 1979).
2. J. Browning, *How to Work with the Spectroscope. A Manual of Practical Manipulation with Spectroscopes of All Kinds* (Browning, 1882).
3. F. Theilmann and S. Grusche, "An RGB approach to prismatic colours," Phys. Educ. **48**, 750–759 (2013).
4. J.-P. Meyn, "Colour mixing based on daylight," Eur. J. Phys. **29**, 1017–1031 (2008).
5. N. Pahlevan, Z. Lee, C. Hu, and J. R. Schott, "Diurnal remote sensing of coastal/oceanic waters: a radiometric analysis for geostationary coastal and air pollution events," Appl. Opt. **53**, 648–665 (2014).
6. K. Chance, "Spectroscopic needs for atmospheric pollution measurements from space," in *AIP Conference Proceedings*, E. Roueff, ed. (AIP, 2007), pp. 13–18.
7. M.-F. Nieva and S. Simón-Díaz, "The chemical composition of the Orion star forming region," Astron. Astrophys. **532**, A2 (2011).
8. A. Cortesi, M. Arnaboldi, L. Coccato, M. R. Merrifield, O. Gerhard, S. Bamford, A. J. Romanowsky, N. R. Napolitano, N. G. Douglas, K. Kuijken, M. Capaccioli, K. C. Freeman, A. L. Chies-Santos, and V. Pota, "The Planetary Nebula Spectrograph survey of S0 galaxy kinematics," Astron. Astrophys. **549**, A115 (2013).

9. P. Figueira, F. Pepe, C. H. F. Melo, N. C. Santos, C. Lovis, M. Mayor, D. Queloz, A. Smette, and S. Udry, “Radial velocities with CRIRES,” Astron. Astrophys. **511**, A55 (2010).
10. M. Franz and R. Schlichenmaier, “The velocity fields of sunspot penumbrae,” Astron. Astrophys. **508**, 1453–1460 (2009).
11. W. W. Luo and H. J. Gerritsen, “Seeing the Fraunhofer lines with only a diffraction grating and a slit,” Am. J. Phys. **61**, 632–635 (1993).
12. K. Thompson, “An easy-to-build spectroscope,” Phys. Educ. **31**, 382–385 (1996).
13. J. Nemechek, “OSA E-Day 2008: a simple spectroscope,” https://www.youtube.com/watch?v=jaoEmc7kQSI.
14. Z. J. Smith, K. Chu, A. R. Espenson, M. Rahimzadeh, A. Gryshuk, M. Molinaro, D. M. Dwyre, S. Lane, D. Matthews, and S. Wachsmann-Hogju, “Cell-phone-based platform for biomedical device development and education applications,” PlosOne **6**, e1570 (2011).
15. R. D. Lorenz, “A simple webcam spectrograph,” Am. J. Phys. **82**, 169–173 (2014).
16. J. J. Lunazzi, “Holophotography with a diffraction grating,” Opt. Eng. **29**, 15–18 (1990).
17. M. Müller and L.-H. Schön, “Virtuelle Beugungsbilder am Gitter,” in *Didaktik der Physik. Frühjahrstagung Münster*, H. Groetzebach and V. Nordmeier, eds. (PhyDid B, 2011) pp. 1–9.
18. J. Dong and W. Zhang, “Imaging of virtual objects with a plane periodic grating,” Opt. Lett. **34**, 3232–3234 (2009).
19. S. Grusche, “Spectral synthesis provides two-dimensional videos on a one-dimensional screen with 360°-visibility and mirror-immunity,” Appl. Opt. **53**, 674–684 (2014).
20. J. J. Lunazzi and N. I. R. Rivera, “Pseudoscopic imaging in a double diffraction process with a slit,” Opt. Express **10**, 1368–1373 (2002).
21. J. J. Lunazzi and N. I. R. Rivera, “Pseudoscopic imaging in a double diffraction process with a slit: critical point properties,” J. Opt. Soc. Am. A **23**, 1021–1026 (2006).
22. J. J. Lunazzi, N. I. R. Rivera, and D. S. F. Magalhães, “Imaging with two spiral diffracting elements intermediated by a pinhole,” J. Opt. Soc. Am. A **25**, 1091–1097 (2008).
23. J. J. Lunazzi and N. I. R. Rivera, “3D imaging with a linear light source,” in *AIP Conference Proceedings*, N. U. Wetter and J. Frejlich, eds. (AIP, 2008), pp. 677–680.
24. S. Benton, “Hologram reconstructions with extended incoherent sources,” J. Opt. Soc. Am. **59**, 1545–1546 (1969).
25. R. Sato and K. Murata, “Cylindrical rainbow hologram,” Appl. Opt. **24**, 2161–2165 (1985).
26. M. Vannoni, V. Greco, and G. Molesini, “One-step 360° rainbow holography with two spherical mirrors,” Appl. Opt. **40**, 633–635 (2001).
27. B. J. Jackin and T. Yatagai, “360° reconstruction of a 3D object using cylindrical computer generated holography,” Appl. Opt. **50**, H147–H152 (2011).
28. M. A. Bershady, “3D spectroscopic instrumentation,” in *3D Spectroscopy in Astronomy*, E. Mediavilla, S. Arribas, M. Roth, J. Cepa-Nogué, and F. Sánchez, eds. (Cambridge University, 2010), pp. 87–125.
29. M. Gunn, D. Barnes, C. R. Cousins, D. Langstaff, L. Tyler, S. Pugh, D. Pullan, and A. D. Griffiths, “A method of extending the capabilities of multispectral interference-filter cameras for planetary exploration and similar applications,” in *Proceedings of University of Strathclyde's Second Annual Academic Hyperspectral Imaging Conference*, S. Marshall, ed. (University of Strathclyde, 2012), pp. 108–113.
30. N. Tack, A. Lambrechts, P. Soussan, and L. Haspeslagh, “A compact, high-speed, and low-cost hyperspectral imager,” Proc. SPIE **8266**, 82660Q (2012).
31. B. Delauré, B. Michiels, J. Biesemans, S. Livens, and T. Van Achteren, “The geospectral camera: a compact and geometrically precise hyperspectral and high spatial resolution imager,” in *ISPRS Archives*, C. Heipke, K. Jacobsen, F. Rottensteiner, and U. Sörgel, eds., Volume **XL-1/W1** (ISPRS, 2013), pp. 69–74.
32. A. Abramov, L. Minai, and D. Yelin, “Spectrally encoded spectral imaging,” Opt. Express **19**, 6913–6922 (2011).
33. M. A. Bershady, Department of Astronomy, University of Wisconsin, 475 North Charter Street, Madison, Wisconsin 53706 (personal communication, 2014).
34. N. Hagan and M. W. Kudenov, “Review of snapshot spectral imaging technologies,” Opt. Eng. **52**, 090901 (2013).
35. Q. Li, X. He, Y. Wang, H. Liu, D. Xu, and F. Guo, “Review of spectral imaging technology in biomedical engineering: achievements and challenges,” J. Biomed. Opt. **18**, 100901 (2013).
36. G. Lu and B. Fei, “Medical hyperspectral imaging: a review,” J. Biomed. Opt. **19**, 010901 (2014).
37. Z. Xiong, D.-W. Sun, X.-A. Zeng, and A. Xie, “Recent developments of hyperspectral imaging systems and their applications in detecting quality attributes of red meats: a review,” J. Food Eng. **132**, 1–13 (2014).
38. G. Høye and A. Fridman, “Mixel camera: a new push-broom camera concept for high spatial resolution keystone-free hyperspectral imaging,” Opt. Express **21**, 11057–11077 (2013).